

1 An orally bioavailable broad-spectrum antiviral inhibits SARS-CoV-2 and multiple  
2 endemic, epidemic and bat coronavirus

3  
4 Timothy P. Sheahan<sup>1\*</sup>, Amy C. Sims<sup>1\*</sup>, Shuntai Zhou<sup>2</sup>, Rachel L. Graham<sup>1</sup>, Collin S.  
5 Hill<sup>2</sup>, Sarah R. Leist<sup>1</sup>, Alexandra Schäfer<sup>1</sup>, Kenneth H. Dinnon III<sup>1</sup>, Stephanie A.  
6 Montgomery<sup>3</sup>, Maria L. Agostini<sup>4</sup>, Andrea J. Pruijssers<sup>4</sup>, James D. Chapell<sup>4</sup>, Ariane J.  
7 Brown<sup>1</sup>, Gregory R. Bluemling<sup>5,6</sup>, Michael G. Natchus<sup>5</sup>, Manohar Saindane<sup>5</sup>, Alexander  
8 A. Kolykhalov<sup>5,6</sup>, George Painter<sup>5,6,7</sup>, Jennifer Harcourt<sup>8</sup>, Azaibi Tamin<sup>8</sup>, Natalie J.  
9 Thornburg<sup>8</sup>, Ronald Swanstrom<sup>2,9</sup>, Mark R. Denison<sup>4</sup>, Ralph S. Baric<sup>1,10</sup>

10

11 <sup>1</sup>Department of Epidemiology, University of North Carolina at Chapel Hill, Chapel Hill, NC

12 <sup>2</sup>Lineberger Comprehensive Cancer Center, University of North Carolina at Chapel Hill,  
13 Chapel Hill, NC

14 <sup>3</sup>Department of Pathology & Laboratory Medicine, University of North Carolina, Chapel  
15 Hill, NC

16 <sup>4</sup>Department of Pediatrics, Vanderbilt University Medical Center, Nashville, TN

17 <sup>5</sup>Emory Institute of Drug Development (EIDD), Emory University, Atlanta, GA

18 <sup>6</sup>Drug Innovation Ventures at Emory (DRIVE), Atlanta, GA

19 <sup>7</sup>Department of Pharmacology and Chemical Biology, Emory University, Atlanta, GA

20 <sup>8</sup>Centers for Disease Control and Prevention, Division of Viral Diseases Atlanta GA

21 <sup>9</sup>Department of Biochemistry and Biophysics, University of North Carolina at Chapel Hill,  
22 Chapel Hill, NC

23 <sup>10</sup>Department of Microbiology and Immunology, University of North Carolina at Chapel  
24 Hill, Chapel Hill, NC

25 \*Authors contributed equally.

26

## 27 **Abstract (153)**

28 Coronaviruses (CoVs) traffic frequently between species resulting in novel disease  
29 outbreaks, most recently exemplified by the newly emerged SARS-CoV-2. Herein, we  
30 show that the ribonucleoside analog  $\beta$ -D-N<sup>4</sup>-hydroxycytidine (NHC, EIDD-1931) has  
31 broad spectrum antiviral activity against SARS-CoV 2, MERS-CoV, SARS-CoV, and

32 related zoonotic group 2b or 2c Bat-CoVs, as well as increased potency against a  
33 coronavirus bearing resistance mutations to another nucleoside analog inhibitor. In  
34 mice infected with SARS-CoV or MERS-CoV, both prophylactic and therapeutic  
35 administration of EIDD-2801, an orally bioavailable NHC-prodrug ( $\beta$ -D-N<sup>4</sup>-  
36 hydroxycytidine-5'-isopropyl ester), improved pulmonary function, and reduced virus  
37 titer and body weight loss. Decreased MERS-CoV yields *in vitro* and *in vivo* were  
38 associated with increased transition mutation frequency in viral but not host cell RNA,  
39 supporting a mechanism of lethal mutagenesis. The potency of NHC/EIDD-2801 against  
40 multiple coronaviruses, its therapeutic efficacy, and oral bioavailability *in vivo*, all  
41 highlight its potential utility as an effective antiviral against SARS-CoV-2 and other  
42 future zoonotic coronaviruses.

43

#### 44 **Introduction**

45 The genetically diverse *Orthocoronavirinae* (coronavirus, CoV) family circulates  
46 in many avian and mammalian species. Phylogenetically, CoVs are divided into 4  
47 genera: alpha (group 1), beta (group 2), gamma (group 3) and delta (group 4). Three  
48 new human CoV have emerged in the past 20 years with severe acute respiratory  
49 syndrome CoV (SARS-CoV) in 2002, Middle East respiratory syndrome CoV (MERS-  
50 CoV) in 2012, and now SARS-CoV-2 in 2019<sup>1-3</sup>. The ongoing SARS-CoV-2 epidemic  
51 (referred to as COVID-19, Coronavirus disease 2019) has caused over 89,000  
52 infections and over 3,000 deaths in 71 countries. Like SARS- and MERS-CoV, the  
53 respiratory disease caused by SARS-CoV-2 can progress to acute lung injury (ALI), an  
54 end stage lung disease with limited treatment options and very poor prognoses<sup>3-5</sup>. This  
55 emergence paradigm is not limited to humans. A novel group 1 CoV called swine acute  
56 diarrhea syndrome CoV (SADS-CoV) recently emerged from bats causing the loss of  
57 over 20,000 pigs in Guangdong Province, China<sup>6</sup>. More alarmingly, many group 2  
58 SARS-like and MERS-like coronaviruses are circulating in bat reservoir species that can  
59 use human receptors and replicate efficiently in primary human lung cells without  
60 adaptation<sup>6-9</sup>. The presence of these “pre-epidemic” zoonotic strains foreshadow the  
61 emergence and epidemic potential of additional SARS-like and MERS-like viruses in the  
62 future. Given the diversity of CoV strains in zoonotic reservoirs and a penchant for

63 emergence, broadly active antivirals are clearly needed for rapid response to new CoV  
64 outbreaks in humans and domesticated animals.

65 Currently, there are no approved therapies specific for any human CoV.  $\beta$ -D-N4-  
66 hydroxycytidine (NHC, EIDD-1931) is orally bioavailable ribonucleoside analog with  
67 broad-spectrum antiviral activity against various unrelated RNA viruses including  
68 influenza, Ebola, CoV and Venezuelan equine encephalitis virus (VEEV)<sup>10-13</sup>. For VEEV,  
69 the mechanism of action (MOA) for NHC has been shown to be through lethal  
70 mutagenesis where deleterious transition mutations accumulate in viral RNA<sup>11,14</sup>. Here,  
71 we demonstrate that NHC exerts potent, broad-spectrum activity against SARS-CoV,  
72 MERS-CoV and their related bat-CoV in primary human airway epithelial cell cultures  
73 (HAE), a biologically relevant model of the human conducting airway. In addition, we  
74 show that NHC is potently antiviral against the newly emerging SARS-CoV-2 as well as  
75 against coronavirus bearing resistance mutations to the potent nucleoside analog  
76 inhibitor, remdesivir (RDV). In SARS- or MERS-CoV infected mice, both prophylactic  
77 and therapeutic administration EIDD-2801, an oral NHC-prodrug ( $\beta$ -D-N<sup>4</sup>-  
78 hydroxycytidine-5'-isopropyl ester) improved pulmonary function and reduced virus titer  
79 and ameliorated disease severity. In addition, therapeutic EIDD-2801 reduced the  
80 pathological features of ALI in SARS-CoV infected mice. Using a high-fidelity deep  
81 sequencing approach (Primer ID), we found that increased mutation rates coincide with  
82 decreased MERS-CoV yields *in vitro* and protective efficacy *in vivo* supporting the MOA  
83 of lethal mutagenesis against emerging CoV<sup>13</sup>. The broad activity and therapeutic  
84 efficacy of NHC/EIDD-2801 highlight its potential to diminish epidemic disease today  
85 and limit future emerging CoV outbreaks.

86

## 87 **Results**

### 88 **NHC potently Inhibits MERS-CoV, SARS-CoV and newly emerging SARS-CoV-2** 89 **Replication.**

90 To determine whether NHC blocks the replication of highly pathogenic human  
91 CoV, we performed antiviral assays in continuous and primary human lung cell cultures.  
92 We first assessed the antiviral activity of NHC against MERS-CoV in the human lung  
93 epithelial cell line Calu-3 2B4 (“Calu3” cells). Using a recombinant MERS-CoV

94 expressing nanoluciferase (MERS-nLUC)<sup>15</sup>, we measured virus replication in cultures  
95 exposed to a dose range of drug for 48hr. NHC was potently antiviral with an average  
96 half-maximum effective concentration (IC<sub>50</sub>) of 0.15 $\mu$ M and no observed cytotoxicity in  
97 similarly treated uninfected cultures across the dose range (50% cytotoxic  
98 concentration, CC<sub>50</sub>, >10 $\mu$ M) (Fig. 1A). The therapeutic index for NHC was >100.  
99 Similarly, NHC strongly inhibited SARS-CoV-2 replication in Vero cells with an IC<sub>50</sub> of  
100 0.3 $\mu$ M and CC<sub>50</sub> of >10 $\mu$ M (Fig. 1B). Human primary airway epithelial (HAE) cell  
101 cultures model the architecture and cellular complexity of the conducting airway and are  
102 readily infected by multiple human and zoonotic CoV, including SARS- and MERS-  
103 CoV<sup>16</sup>. We first assessed cytotoxicity of NHC in HAE treated with an extended dose  
104 range for 48hr using quantitative PCR of cell death-related gene transcripts as our  
105 metric. NHC treatment did not appreciably alter gene expression even at doses up to  
106 100 $\mu$ M (Supplementary Figure 1). In MERS-CoV infected HAE, NHC dramatically  
107 reduced virus production with maximal titer reduction of > 5 logs at 10 $\mu$ M (average IC<sub>50</sub>  
108 = 0.024  $\mu$ M), which correlated with reduced genomic (ORF1) and subgenomic (ORFN)  
109 RNA in paired samples (Fig. 1C). We observed similar trends in titer reduction (> 3 log  
110 at 10 $\mu$ M, average IC<sub>50</sub> = 0.14  $\mu$ M) and levels of genomic and subgenomic RNA in  
111 SARS-CoV infected HAE (Fig. 1D). Thus, NHC was potently antiviral against MERS-  
112 CoV and SARS-CoV-2 in cell lines and MERS-CoV and SARS-CoV in human primary  
113 HAE cell cultures without cytotoxicity.

114

115 **NHC is effective against remdesivir resistant virus and multiple distinct zoonotic  
116 CoV.**

117 All human CoV are thought to have emerged as zoonoses most recently  
118 exemplified by SARS-CoV, MERS-CoV and SARS-CoV-2<sup>17-19</sup>. Although taxonomically  
119 divided into multiple genogroups (alpha, beta, gamma, delta), human CoV are found  
120 in only the alpha and beta subgroups thus far (Fig. 2A). There is high sequence  
121 conservation in the RdRp across CoV (Fig. 2A). For example, the RdRp of SARS-CoV-2  
122 has 99.1% similarity and 96% amino acid identity to that of SARS-CoV (Fig. 2A). To  
123 gain insight into structural conservation of RdRp across the CoV family, we modeled the  
124 variation reflected in the RdRp dendrogram in Fig. 2A onto the structure of the SARS-

125 CoV RdRp<sup>20</sup> (Fig. 2B). The core of the RdRp molecule and main structural motifs that all  
126 RdRp harbor (Fig. 2B and Supplementary Figure 2) are highly conserved among CoV  
127 including SARS-CoV-2. We previously reported that CoV resistance to another broad  
128 spectrum nucleoside analog, remdesivir (RDV) was mediated by RdRp residues F480L  
129 and V557L in a model coronavirus mouse hepatitis virus (MHV) and in SARS-CoV,  
130 resulting in a 5-fold shift in IC<sub>50</sub> (Fig. 2C)<sup>21</sup>. Consequently, we tested whether RDV  
131 resistance mutations in MHV conferred cross resistance to NHC (Figure 2D). In fact,  
132 the two RDV resistance mutations, alone or together conferred increased sensitivity to  
133 inhibition by NHC. As our previous studies have demonstrated a high genetic barrier to  
134 NHC for VEEV, influenza and coronavirus<sup>11-13</sup>, the lack of cross resistance further  
135 suggests that NHC and RDV may select for exclusive and mutually sensitizing  
136 resistance pathways.

137 To explore the breadth of antiviral efficacy against zoonotic CoV, we performed  
138 antiviral assays in HAE with three zoonotic Bat-CoV, SHC014, HKU3 and HKU5.  
139 Closely related to the beta 2b SARS-CoV, Bat-CoV SHC014 is capable of replicating in  
140 human cells without adaptation<sup>8</sup> suggesting its potential for zoonotic emergence. More  
141 distantly related SARS-like beta 2b CoV, recombinant Bat-CoV HKU3 has a modified  
142 receptor binding domain to facilitate growth in cell culture<sup>22</sup>. Lastly, Bat-CoV HKU5 is a  
143 MERS-like beta 2c CoV<sup>23</sup>. NHC diminished infectious virus production and the levels of  
144 genomic/subgenomic viral RNA in HAE in a dose-dependent manner for all three Bat-  
145 CoVs (Fig. 3). Therefore, the antiviral activity of NHC was not limited by natural amino  
146 acid variation in the RdRp, which among the group 2b and group 2c CoV can vary by  
147 almost 20% (Fig. 2A). Moreover, these data suggest that if another SARS- or MERS-  
148 like virus were to spillover into humans in the future, they would likely be susceptible to  
149 the antiviral activity of NHC.

150

### 151 **NHC antiviral activity is associated with increased viral mutation rates.**

152 It has recently been shown that NHC treatment increases the mutation rate in  
153 viral genomic RNA of RSV<sup>24</sup>, VEEV<sup>11</sup>, influenza<sup>24</sup>, and our previous study used RNA  
154 seq to show that overall transition mutation frequency is increased during NHC  
155 treatment of MHV and MERS-CoV during infection in continuous cell lines<sup>13</sup>. We sought

156 to determine if NHC would increase the mutation frequency during MERS-CoV infection  
157 in human primary human airway epithelial cells (HAE). Using MERS-CoV infected HAE  
158 treated with either vehicle or a dose range of NHC or RDV, we show that both drugs  
159 reduced virus titers in a dose-dependent manner (Fig. 4A). We then employed a highly-  
160 sensitive high-fidelity deep sequencing approach (Primer ID NGS), which uses  
161 barcoded degenerate primers and Illumina indexed libraries to determine accurate  
162 mutation rates after antiviral treatment on viral RNA production<sup>25</sup>. Using this approach,  
163 we analyzed a 538bp region of viral genomic RNA in nonstructural protein 15 (nsp15).  
164 The error rates (#mutations/10,000 bases) in vehicle (0.01) or RDV (0.01) treated  
165 cultures were very low. RDV is reported to act via chain termination of nascent viral  
166 RNA, and thus the low error rates in RDV-treated cultures are in line with the proposed  
167 MOA<sup>26</sup>. In contrast, the error rate was significantly increased in NHC-treated MERS-  
168 CoV RNA in a dose-dependent manner (10-fold at 10 $\mu$ M and 5-fold at 1 $\mu$ M) at both 24  
169 and 48hpi (Fig. 4C). The magnitude of the error rate in NHC-treated cultures correlated  
170 with virus titer reduction. At 48hpi the respective error rate and virus titer was 0.015 and  
171 3.96E+06 pfu/mL for vehicle treatment, 0.045 and 2.86E+04 pfu/mL with 1 $\mu$ M NHC; and  
172 0.090 and 1.5E+02 pfu/mL 10 $\mu$ M NHC. Thus, with 1 $\mu$ M NHC a 3-fold increase in error  
173 rate resulted in a 138-fold decrease in virus titer, while with 10 $\mu$ M NHC a 6-fold increase  
174 in error rate resulted in a 26,000-fold decrease in virus titer.

175 We then examined the mutational spectra induced by NHC, which can be  
176 incorporated into viral RNA as a substitution for either cytosine (C) or Uridine (U). RNA-  
177 mutagenic antivirals may incorporate in both nascent negative and positive sense RNA  
178 during genome replication (Fig. 4D). Adenine-to-guanine (A-to-G) and uracil-to-cytosine  
179 (U-to-C) transitions were enriched in MERS-CoV genomic RNA in an NHC dose-  
180 dependent manner (Fig. 4E). Collectively, these data used high-fidelity sequence  
181 analysis to demonstrate a specific enrichment for A:G and C:U transitions in MERS-  
182 CoV RNA after NHC treatment of primary HAE cell cultures.

183

#### 184 **Therapeutic EIDD-2801 reduces SARS-CoV replication and pathogenesis.**

185 Given the promising antiviral activity of NHC in vitro, we next evaluated its *in vivo*  
186 efficacy using EIDD-2801, an orally bioavailable prodrug of NHC ( $\beta$ -D-N<sup>4</sup>-

187 hydroxycytidine-5'-isopropyl ester), designed for improved *in vivo* pharmacokinetics and  
188 oral bioavailability in humans and non-human primates<sup>12</sup>. Importantly, the plasma  
189 profiles of NHC and EIDD-2801 were similar in mice following oral delivery<sup>12</sup>. We first  
190 performed a prophylactic dose escalation study in C57BL/6 mice where we orally  
191 administered vehicle (10% PEG, 2.5% Cremophor RH40 in water) or 50, 150 or 500  
192 mg/kg EIDD-2801 2hr prior to intranasal infection with 5E+04 PFU of mouse-adapted  
193 SARS-CoV (SARS-MA15), and then every 12hr thereafter. Beginning on 3dpi and  
194 through the end of the study, body weight loss compared to vehicle treatment was  
195 significantly diminished (50mg/kg) or prevented (150, 500mg/kg) with EIDD-2801  
196 prophylaxis ( $P < 0.0001$ ) (Supplemental Figure 2A). Lung hemorrhage was also  
197 significantly reduced 5dpi with 500mg/kg EIDD-2801 treatment (Supplemental Figure  
198 2B). Interestingly, there was a dose-dependent reduction in SARS-CoV lung titer  
199 (median titers: 50mg/kg = 7E+03 pfu/mL, 150mg/kg = 2.5E+03 pfu/mL, 500mg/kg = 50  
200 pfu/mL, vehicle = 6.5E+04 pfu/mL) with significant differences among the vehicle, 150  
201 mg/kg ( $P = 0.03$ ) and 500mg/kg ( $P = 0.006$ ) groups. Thus, prophylactic orally  
202 administered EIDD-2801 was robustly antiviral and able to prevent SARS-CoV  
203 replication and disease.

204 Since only the 500mg/kg group significantly diminished weight loss, hemorrhage  
205 and reduced lung titer to near undetectable levels, we tested this dose under  
206 therapeutic treatment conditions to determine if EIDD-2801 could improve the outcomes  
207 of an ongoing CoV infection. As a control, we initiated oral vehicle or EIDD-2801 2hr  
208 prior to infection with 1E+04 pfu SARS-MA15. For therapeutic conditions, we initiated  
209 EIDD-2801 treatment 12, 24, or 48hr after infection. After initiating treatment, dosing for  
210 all groups was performed every 12hr for the duration of the study. Both prophylactic  
211 treatment initiated 2hr prior to infection and therapeutic treatment initiated 12hr after  
212 infection significantly prevented body weight loss following SARS-CoV infection on 2dpi  
213 and thereafter (-2hr:  $P = 0.0002$  to  $<0.0001$ ; +12hr:  $P = 0.0289$  to  $<0.0001$ ) (Fig. 5A).  
214 Treatment initiated 24hpi also significantly reduced body weight loss (3-5dpi,  $P = 0.01$  to  
215  $<0.0001$ ) although not to the same degree as the earlier treatment initiation groups.  
216 When initiated 48hpi, body weight loss was only different from vehicle on 4dpi ( $P =$   
217 0.037, Fig. 5A). Therapeutic EIDD-2801 significantly reduced lung hemorrhage when

218 initiated up to 24hr after infection mirroring the body weight loss phenotypes (Fig. 5B).  
219 Interestingly, all EIDD-2801 treated mice had significantly reduced viral loads in the  
220 lungs even in the +48hr group (Fig. 5C), which experienced the least protection from  
221 body weight loss and lung hemorrhage. We also measured pulmonary function via  
222 whole body plethysmography (WPB). In Figure 5D, we show the WBP PenH metric,  
223 which is a surrogate marker for bronchoconstriction or pulmonary obstruction<sup>27</sup>, was  
224 significantly improved throughout the course of the study if treatment was initiated up to  
225 12hr after infection, although the +24hr group showed sporadic improvement as well  
226 (Fig. 5D). Lastly, we blindly evaluated hematoxylin and eosin stained lung tissue  
227 sections for histological features of ALI using two different and complementary scoring  
228 tools<sup>15</sup>, which show that treatment initiated up to +12hr significantly reduced ALI (Fig.  
229 5E). Altogether, therapeutic EIDD-2801 was potently antiviral against SARS-CoV *in vivo*  
230 but the degree of clinical benefit was dependent on the time of initiation post infection.  
231

232 **Prophylactic and therapeutic EIDD-2801 reduces MERS-CoV replication and  
233 pathogenesis.**

234 After obtaining promising *in vivo* efficacy data with SARS-CoV, we investigated  
235 whether EIDD-2801 would be effective against MERS-CoV. As the murine ortholog of  
236 the MERS-CoV receptor, dipeptidyl peptidase 4 (DPP4), does not support viral binding  
237 and entry, all *in vivo* studies were performed in genetically modified mice encoding a  
238 murine DPP4 receptor encoding two human residues at positions 288 and 330 (hDPP4  
239 288/330 mice)<sup>15,28</sup>. Similar to our SARS-CoV data (Supplementary Figure 3), all doses  
240 of prophylactic EIDD-2801 (50, 150 and 500mg/kg) protected hDPP4 288/330 mice  
241 from significant body weight loss ( $P = 0.03$  to  $< 0.0001$ ), lung hemorrhage ( $P = 0.01$  to  
242  $<0.0001$ ), and virus replication which was undetectable ( $P < 0.0001$ ) regardless of drug  
243 dose following intranasal infection with 5E+04 PFU mouse-adapted MERS-CoV  
244 (Supplementary Figure 4).

245 We then evaluated the therapeutic efficacy EIDD-2801 following the promising  
246 results of our prophylactic studies. Similar to our SARS-CoV study, EIDD-2801  
247 treatment administered before or 12hr after intranasal mouse-adapted MERS-CoV  
248 infection (5E+04 PFU) prevented body weight loss from 2 through 6dpi (Fig. 6A,  $P =$

249 0.02 to <0.0001) and lung hemorrhage on 6dpi (Fig. 6B,  $P = 0.0004$  to <0.0001), but  
250 treatment initiated 24 or 48hr did not offer similar protection. Unlike body weight loss  
251 and lung hemorrhage data which varied by treatment initiation time, virus lung titer on  
252 6dpi was significantly reduced to the limit of detection in all treatment groups (Fig. 6C,  $P$   
253 <0.0001). Interestingly, when viral genomic RNA was quantified in paired samples of  
254 lung tissue, EIDD-2801 significantly reduced levels of viral RNA ( $P < 0.0001$  to 0.017) in  
255 an initiation time-dependent manner for all groups except for +48hr (Fig. 6D). The  
256 discrepancy among infectious titers and viral RNA suggests that accumulated mutations  
257 render the particles non-infectious and undetectable by plaque assay consistent with  
258 the MOA. To gauge the effect of EIDD-2801 treatment on lung function, we assessed  
259 pulmonary function by WBP. Mirroring the body weight loss data, normal pulmonary  
260 function was only observed in groups where treatment was initiated prior to or 12hr after  
261 infection (Fig. 6E). Collectively, these data demonstrate that NHC prodrug, EIDD-2801,  
262 robustly reduces MERS-CoV infectious titers, viral RNA, and pathogenesis under both  
263 prophylactic and therapeutic conditions.

264

265 **Therapeutic efficacy correlates with an increased MERS-CoV mutation rate in**  
266 ***vivo*, without increased mutations in cellular RNA.**

267 To study the molecular mechanisms associated with drug performance *in vivo*,  
268 we investigated the correlation between infectious virus production and EIDD-2801-  
269 mediated mutagenesis of MERS-CoV RNA under therapeutic treatment conditions.  
270 Using Primer ID NGS, we measured the mutation rates of both viral genomic RNA (i.e.  
271 non-structural protein 10, nsp10) and host interferon stimulated gene 15 (ISG15)  
272 mRNA, a highly upregulated innate immune related gene after MERS-CoV infection  
273 (Fig. 6F). Primer ID NGS measures the mutational frequency in single RNA molecules  
274 each of which are represented by a single template consensus sequence (TCS, See  
275 Fig. 4B)<sup>25</sup>. Viral TCS were significantly reduced in a treatment initiation time-dependent  
276 manner (Fig. 6G) similar to viral genomic RNA measured by qRT-PCR (Fig. 6D). In  
277 contrast, the numbers of ISG15 TCS were similar ( $P = 0.2$  to 0.8) for all groups  
278 indicating that neither vehicle nor drug treatment significantly affected the levels of or  
279 mutated ISG15 mRNA transcripts (Fig. 6G). Similar to our TCS data in Figure 6G, the

280 total error rate in viral nsp10 was significantly increased in groups where treatment was  
281 initiated prior to (-2hr, median error rate = 10.5 errors/10,000 bases,  $P < 0.0001$ ) and up  
282 to 24hr post infection (12hr, median error rate = 8.2 errors/10,000 bases,  $P < 0.0001$  ;  
283 +24hr, median error rate = 5.4 errors/10,000 bases,  $P = 0.0003$ ) but the error rates in  
284 ISG15 remained at baseline for all groups (Fig. 6H). In addition, nucleotide transitions  
285 observed in MERS-CoV genomes in vitro (i.e. C to U transitions, Fig. 3), were also  
286 observed *in vivo* in groups where treatment was initiated prior to and up to 12hr post  
287 infection ( $P = 0.0003$  to  $< 0.0001$ ) (Fig. 5I). Importantly, these transitions were not  
288 observed in host ISG15 mRNA (Fig. 5I). Lastly, the EIDD-2801 dose-dependent  
289 mutagenesis of viral RNA correlated with an increase in codon change frequency,  
290 including stop codons, in mice where treatment was initiated 12hr or before (vehicle  
291 median = 3.4; -2hr median = 22.8,  $P = 0.0035$ ; +12hr median = 20.0,  $P = 0.0004$ , Fig.  
292 5I). Thus, approximately 20% of the mutations observed in the -2hr and +12hr groups  
293 resulted in a codon change and alteration of the nsp10 protein sequence. When  
294 extrapolating our results from nsp10 to the entirety of the 30kb MERS-CoV genome,  
295 EIDD-2801 likely causes between 15 (+24hr treatment) and 30 (-2hr treatment)  
296 mutations per genome 10-20% of which result in amino acid coding changes.  
297 Altogether, our data demonstrates that EIDD-2801-driven mutagenesis correlates well  
298 with the reductions in viral load, strongly suggestive of an error catastrophe-driven  
299 mechanism of action under therapeutic conditions.

300

## 301 **Discussion**

302 In the past 20 years, three novel human coronaviruses have emerged<sup>29,30</sup>. The  
303 group 2b SARS-like CoV represent an existential and future threat to global health as  
304 evidenced by the emergence of SARS-CoV and SARS-CoV2 and zoonotic SARS-like  
305 bat CoV strains that can use human ACE2 receptors, grow well in primary human  
306 airway cells and vary by as much as 25% in key therapeutic and vaccine gene  
307 targets<sup>8,31</sup>. Thus, to address the current public health emergency of COVID-19 and to  
308 maximize pandemic preparedness in the future, broad-based vaccines and  
309 therapeutics, which are active against the higher risk RNA virus families prone to  
310 emergence are desperately needed.

311        We recently reported the broad-spectrum potency of the nucleoside prodrug,  
312 remdesivir (RDV), against an array of epidemic, contemporary and zoonotic CoV both in  
313 vitro and *in vivo*<sup>15,16,21,31</sup>. Currently RDV therapeutic efficacy is under investigation in  
314 several human clinical trials in China, the United States and elsewhere<sup>32</sup>. Here, we  
315 report the broad-spectrum antiviral activity of NHC and its orally bioavailable prodrug  
316 EIDD-2801, against SARS-CoV, MERS-CoV and related bat-CoV in primary human  
317 airway epithelial cells, as well as against the current pandemic strain SARS-CoV-2. In  
318 addition, NHC is broadly active against multiple genetically distinct viruses including  
319 coronaviruses, Venezuelan equine encephalitis (VEE), influenza A and B, Ebola, and  
320 Chikungunya viruses<sup>10-13,16,21,24,33-35</sup>. Here, we show that prophylactic and therapeutic  
321 EIDD-2801 significantly reduced lung viral loads and improved pulmonary function in  
322 mouse models of both SARS- and MERS-CoV pathogenesis. Although the  
323 improvement in both SARS- and MERS-CoV outcomes diminished with the increase of  
324 treatment initiation time, it is important to note that the kinetics of disease in mice are  
325 compressed as compared to that in humans. While SARS- and MERS-CoV lung titers  
326 peak on 2dpi in mice concurrent with the onset of clinical signs and notable damage to  
327 the lung epithelium, in humans this occurs 7-10 days after the onset of  
328 symptoms<sup>16,28,36,37</sup>. Thus, in mice, the window within which to treat emerging CoV  
329 infection prior to peak replication is compressed (e.g., 24-48hr) but should be much  
330 longer in humans. Although speculative, the SARS- and MERS-CoV *in vivo* data  
331 provided herein suggest that 2019-nCoV will prove highly vulnerable to NHC treatment  
332 modalities *in vivo*, critical experiments that must be performed as animal models  
333 become available. The data provided in this manuscript suggest that NHC should be  
334 quickly evaluated in primate models of human disease, using immediate models for  
335 MERS-CoV and SARS-CoV pathogenesis<sup>38,39</sup>.

336        Small molecule antivirals can exert their antiviral effect through multiple  
337 mechanisms including blocking viral entry, inhibiting a virally encoded enzyme, blocking  
338 virus particle formation, or targeting a host factor required for replication<sup>40</sup>. For VEE,  
339 EIDD-2801 exerts its antiviral activity on the RNA-dependent RNA polymerase leading  
340 to error catastrophe by inducing an error rate of replication that surpasses the error  
341 threshold allowed to sustain a virus population<sup>11,12</sup>. This process occurs when NHC is

342 incorporated during RNA synthesis then subsequently misread thus increasing mutation  
343 rates. Therefore, the NHC MOA would appear less likely to be affected by the RNA  
344 proofreading activity encoded by the nsp14 exonuclease function that otherwise limits  
345 misincorporation<sup>41</sup>. Here, we present data using Primer ID NGS, a state of the art deep  
346 sequencing-based approach, to quantitate the frequency and identity of the mutational  
347 spectra in the MERS-CoV genome in both drug treated primary human airway cells and  
348 in mice at single genome resolution<sup>25</sup>. As CoV are positive sense RNA viruses that  
349 replicate through a negative sense RNA intermediate, NHC incorporation as a “C” or a  
350 “U” can occur in both polarities of RNA. Using Primer ID NGS, we found increased  
351 nucleotide transitions (A to G, G to A, C to U, U to C) consistent with those reported  
352 after influenza and VEE infections<sup>11,12</sup>. Under identical conditions, remdesivir did not  
353 alter the mutation rate in MERS-CoV genomic RNA, supporting its reported mechanism  
354 of action as a chain terminator of viral RNA synthesis<sup>26</sup>. In primary human lung cell  
355 cultures and mice infected with MERS-CoV, the NHC mutation rates inversely  
356 correlated with a reduction in infectious virus. In addition, we found a positive correlation  
357 between increased mutation rates and the frequency of nonsynonymous mutations and  
358 the degree of therapeutic efficacy in mice. To explore the potential off-target effect in  
359 host mRNA which may contribute to drug toxicity, we also examined the impact of NHC  
360 treatment on transcripts from the highly MERS-CoV induced interferon stimulated gene  
361 15 (ISG15). While ISG15 is present in great abundance, an accumulation of mutations  
362 was not observed in ISG15 in this model even at 500mg/kg dosing. These data also  
363 support previous studies using RNAseq to demonstrate that the model coronavirus  
364 MHV displayed increased mutation frequencies following NHC treatment *in vitro*<sup>13</sup>. All  
365 together, these data strongly support the notion that EIDD-2801 and its active  
366 nucleoside analog NHC, exert their antiviral effect through the induction of error  
367 catastrophe in the targeted virus. While our data suggest that the MERS-CoV nsp14  
368 proofreading activity appeared ineffective against NHC *in vitro* and EIDD-2801 *in vivo*,  
369 future studies should investigate the antiviral activity of NHC in the presence or absence  
370 of the nsp14 proofreading activity, as loss of this activity increased the sensitivity of  
371 MHV and SARS-CoV replication to remdesivir treatment<sup>41</sup>.

372           Together, our data support the continued development of EIDD-2801 as a potent  
373 broad spectrum antiviral that could be useful in treating contemporary, newly emerged  
374 and emerging coronavirus infections of the future.

375

### 376 **Materials and Methods**

377 **Compounds.** The parental compound  $\beta$ -D-N<sup>4</sup>-hydroxycytidine (NHC, all *in vitro*  
378 studies) and its prodrug EIDD-2801 (all *in vivo* studies) was supplied by Emory  
379 University Institute for Drug Discovery (EIDD). NHC was supplied as a 10mM stock in  
380 DMSO and EIDD-2801 as a solid and solubilized in vehicle containing 10% PEG400,  
381 2.5% Cremophor RH40 in water (10/2.5/87.5%, all v/v) prior to use. Remdesivir (RDV)  
382 was solubilized in 100% DMSO and provided by Gilead Sciences, Inc as previously  
383 described<sup>15,16</sup>.

384 **Virus strains.** All viruses used for these studies were derived from infectious clones  
385 and isolated as previously described<sup>42</sup>. Virus strains for *in vitro* experiments include  
386 SARS-CoV expressing the green fluorescent protein (GFP) in place of open reading  
387 frames 7a/b (ORF7a/b, SARS-GFP)<sup>42</sup>, bat-spike receptor binding domain (Bat-SRBD)<sup>22</sup>  
388 is a chimeric CoV strain derived from the HKU3 SARS-like bat coronavirus genomic  
389 sequence that has the wild type (Urbani SARS-CoV strain) RBD in the HKU3 spike  
390 gene to allow for virus replication in non-human primate cell lines and HAE cultures,  
391 SHC014 SARS-like bat coronavirus<sup>8</sup>, MERS-CoV expressing nanoluciferase in the  
392 place of ORF3 (MERS-nLUC)<sup>16</sup> and MERS-CoV expressing the red fluorescent protein  
393 gene in the place of ORF 5 (RFP, MERS-RFP)<sup>43</sup>. The virus stock utilized for MERS-  
394 CoV *in vivo* studies was derived from a plaque purified isolate of the mouse-adapted  
395 MERS-CoV p35C4 strain<sup>44</sup>. The virus stock utilized for SARS-CoV *in vivo* studies was  
396 derived from the infectious clone of the mouse-adapted SARS-CoV MA15 (MA15)  
397 strain<sup>45</sup>.

398 ***In vitro* experiments Calu3:** At 48hrs prior to infection, Calu3 2B4 cells were plated in a  
399 96-well black walled clear bottom plate at 5x10<sup>4</sup> cells/well. A 10mM stock of NHC was  
400 serially diluted in 100% DMSO in 3-fold increments to obtain a ten-point dilution series.  
401 MERS-nLUC was diluted in DMEM supplemented with 10% FBS, and 1% Antibiotic-

402 Antimycotic to achieve a multiplicity of infection (MOI) of 0.08. Cells were infected and  
403 treated with NHC in triplicate per drug dilution for 1hr, after which viral inoculum was  
404 aspirated, cultures were rinsed once and fresh medium containing drug or vehicle was  
405 added. At 48hrs post infection, nanoluciferase expression as a surrogate for virus  
406 replication was quantitated on a Spectramax (Molecular Devices) plate reader  
407 according to the manufacturer's instructions (Promega, NanoGlo). For our 100%  
408 inhibition control, diluted MERS-nLUC was exposed to short-wave UV light (UVP, LLC)  
409 for 6 minutes to inhibit the ability of the virus to replicate. For our 0% inhibition control,  
410 cells were infected in the presence of vehicle only. DMSO was kept constant in all  
411 conditions at 0.05%. Values from triplicate wells per condition were averaged and  
412 compared to controls to generate a percent inhibition value for each drug dilution. The  
413 IC<sub>50</sub> value was defined as the concentration at which there was a 50% decrease in  
414 luciferase expression. Data was analyzed using GraphPad Prism 8.0 (La Jolla, CA).  
415 The IC<sub>50</sub> values were calculated by non-linear regression analysis using the dose-  
416 response (variable slope) equation (four parameter logistic equation): Y = Bottom +  
417 (Top-Bottom)/(1+10<sup>((LogIC50-X)\*HillSlope)</sup>). To measure cell viability to determine if  
418 there was any NHC induced cytotoxicity, Calu3 2B4 cells were plated and treated with  
419 NHC only as described above. Cells were exposed to the same ten-point dilution series  
420 created for the in vitro efficacy studies. As above, 0.05% DMSO-treated cells served as  
421 our 0% cytotoxicity control. Wells without cells served as our 100% cytotoxic positive  
422 control. After 48hr, cell viability was measured on a Spectramax (Molecular Devices) via  
423 Cell-Titer Glo Assay (Promega) according to the manufacturer's protocol. Similar data  
424 was obtained in three independent experiments.

425 HAE: Human tracheobronchial epithelial cells were obtained from airway specimens  
426 resected from patients undergoing surgery under University of North Carolina  
427 Institutional Review Board-approved protocols by the Cystic Fibrosis Center Tissue  
428 Culture Core. Primary cells were expanded to generate passage 1 cells and passage 2  
429 cells were plated at a density of 250,000 cells per well on Transwell-COL (12mm  
430 diameter) supports. Human airway epithelium cultures (HAE) were generated by  
431 provision of an air-liquid interface for 6 to 8 weeks to form well-differentiated, polarized  
432 cultures that resembled *in vivo* pseudostratified mucociliary epithelium<sup>46</sup>. At 48 hours

433 prior to infection the apical surface of the culture was washed with 500  $\mu$ L PBS for 1.5  
434 hours at 37°C and the cultures moved into fresh air liquid interface (ALI) media.  
435 Immediately prior to infection, apical surfaces were washed twice with 500  $\mu$ L of PBS  
436 with each wash lasting 30 minutes at 37°C and HAE cultures were moved into ALI  
437 media containing various concentrations of NHC ranging from 10  $\mu$ M to 0.0016  $\mu$ M as  
438 indicated for each experiment (final % DMSO < 0.05%). Upon removing the second  
439 PBS wash, 200  $\mu$ L of viral inoculum (multiplicity of infection of (MOI) 0.5) was added to  
440 the apical surface and HAE cultures were incubated for 3 hours at 37°C. Viral inoculum  
441 was then removed, and the apical surface of the cultures were washed three times with  
442 500 $\mu$ L PBS and then incubated at 37°C until 48 hours post infection (hpi). For all HAE  
443 cultures, infectious virus produced was collected by washing the apical surface of the  
444 culture with 100  $\mu$ L PBS. Apical washes were stored at -80 °C until analysis and titered  
445 by plaque assay as previously described<sup>16</sup>.

446

447 **qRT-PCR approach to assess cytotoxicity:** Total RNA was isolated using the Zymo  
448 Direct-zol RNA MiniPrep Kit (Zymo Research Corp., Irvine, CA, USA) according to the  
449 manufacturer's directions. First-strand cDNA was generated using Superscript III  
450 reverse transcriptase (Life Technologies, Carlsbad, CA, USA). For quantification of  
451 cellular markers of toxicity/apoptosis, real-time PCR was performed using commercially  
452 validated TaqMan-based primer-probe sets (**Supplementary Table 1**) and TaqMan  
453 Universal PCR Mix (Life Technologies). Results were then normalized as described  
454 above.

455

#### 456 **Primer ID and Deep Sequencing**

457 Primer ID NGS is designed to specifically identify and remove RT-PCR mutations, while  
458 facilitating highly accurate sequence determination of single RNA molecules, because  
459 each cDNA is created with a barcoded degenerate primer (N10, 4<sup>10</sup> combinations) from  
460 which Illumina indexed libraries are made. We used a multiplexed Primer ID library prep  
461 approach and MiSeq sequencing to investigate the presence of mutations in the viral  
462 genomes and murine mRNA. We designed cDNA primers targeting multiple regions on  
463 the viral genome and murine mRNA, each with a block of random nucleotides (11 bp

464 long) as the Primer ID<sup>25,47</sup> (**Supplementary Table 2**). Viral RNA was extracted using  
465 QIAamp viral RNA kit. A pre-amplification titration of templates was performed to  
466 estimate the amount of template to use. We used SuperScript III to make cDNA with  
467 multiplexed cDNA primers based on the regions to be sequenced. We used 41R\_PID11  
468 for the pilot sequencing and titration determination. For the MERS-CoV sequencing, we  
469 multiplexed nsp10\_PID11, nsp12\_PID11 and nsp14\_PID11 for the cDNA reaction; for  
470 the murine mRNA sequencing, we used mixed primers of nsp10\_PID11, ifit3\_PID11,  
471 isg15\_PID11. After bead purification, we amplified the cDNA with a mixture of forward  
472 primers (based on the described schemes) and a universal reverse primer, followed by  
473 another round of PCR to incorporate Illumina sequencing adaptors and barcodes in the  
474 amplicons. After gel-purification and quantification, we pooled 24 libraries for MiSeq 300  
475 base paired-end sequencing. The TCS pipeline version 1.38  
476 (<https://github.com/SwanstromLab/PID>) was used to process the Primer ID sequencing  
477 data and construct template consensus sequences (TCSs) to represent each individual  
478 input templates, and the sequences of each region in the pool was de-multiplexed. The  
479 RUBY package viral\_seq version 1.0.6 ([https://rubygems.org/gems/viral\\_seq](https://rubygems.org/gems/viral_seq)) was used  
480 to calculate the mutation rate at each position.

481  
482 **In vivo experiments.** We performed 4 mouse studies to evaluate the *in vivo* efficacy of  
483 the NHC prodrug (EIDD-2801). First, we performed prophylactic dose escalation studies  
484 for both SARS- and MERS-CoV to determine the most efficacious dose of EIDD-2801  
485 per virus. For SARS-CoV, in cohorts of equivalent numbers of male and female 20-29  
486 week old SPF C57BL/6J (Stock 000664 Jackson Labs) mice (n = 10/dose group), we  
487 administered vehicle (10% PEG, 2.5% Cremophor RH40 in water) or 50, 150 or  
488 500mg/kg EIDD-2801 by oral gavage 2hr prior to intranasal infection with 1E+04 PFU  
489 mouse-adapted SARS-CoV strain MA15 in 50µl. Mice were anaesthetized with a  
490 mixture of ketamine/xylazine prior to intranasal infection. Vehicle or drug was  
491 administered every 12hr for the remainder of the study. Body weight and pulmonary  
492 function by whole body plethysmography was measured daily. On 5dpi, animals were  
493 sacrificed by isoflurane overdose, lungs were scored for lung hemorrhage, and the  
494 inferior right lobe was frozen at -80°C for viral titration via plaque assay. Briefly,

495 500,000 Vero E6 cells/well were seeded in 6-well plates. The following day, medium  
496 was removed and serial dilutions of clarified lung homogenate were added per plate (10<sup>-1</sup> to 10<sup>-6</sup> dilutions) and incubated at 37°C for 1hr after which wells were overlayed with  
497 1X DMEM, 5% Fetal Clone 2 serum, 1X antibiotic/antimycotic, 0.8% agarose. Two days  
498 after, plaques were enumerated to generate a plaque/ml value. Lung hemorrhage is a  
499 gross pathological phenotype readily observed by the naked eye driven by the degree  
500 of virus replication where the coloration of the lung changes from pink to dark red<sup>48,49</sup>.  
501 The large left lobe was placed in 10 % buffered formalin and stored at 4°C for 1-3  
502 weeks until histological sectioning and analysis. For MERS-CoV, the prophylactic dose  
503 escalation studies we performed exactly as done for SARS-CoV with the following  
504 exceptions. First, MERS-CoV binds the human receptor dipeptidyl peptidase 4 (DPP4) to  
505 gain entry into cells and two residues (288 and 330) in the binding interface of mouse  
506 DPP4 prevent infection of mice. We recently developed a mouse model for MERS-CoV  
507 through the mutation of mouse DPP4 at 288 and 330 thus humanizing the receptor  
508 (*hDPP4*) and rendering mice susceptible to MERS-CoV infection<sup>28</sup>. We performed all *in*  
509 *vivo* studies with EIDD-2801 in equivalent numbers of 10-14 week old female and male  
510 C57BL/6J *hDPP4* mice. Second, we intranasally infected mice with 5E+04 PFU mouse-  
511 adapted MERS-CoV strain M35C4 in 50µl. Third, to titer lungs by plaque assay, Vero  
512 CCL81 cells were used and plaques were enumerated 3 days post infection.  
513

514 To determine the time at which therapeutic administration of EIDD-2801 would  
515 fail to improve outcomes with SARS-CoV or MERS-CoV infection, we performed  
516 therapeutic efficacy studies in mice where we initiated treatment 2hr prior to infection or  
517 12, 24 or 48hr after infection. As 500mg/kg provided the most complete protection from  
518 disease in prophylactic SARS-CoV studies, this dose was used for both therapeutic  
519 efficacy studies. Vehicle or EIDD-2801 was given via oral gavage twice daily following  
520 initiation of treatment. For both SARS-CoV and MERS-CoV, the infectious dose for the  
521 therapeutic studies and the mouse strains were the same as that used in the  
522 prophylactic studies. The numbers of mice per group for the SARS-CoV studies were as  
523 follows: Vehicle (n = 10), -2hr (n = 10), +12hr (n = 10), +24hr (n = 10), +48hr (n = 10).  
524 The numbers of mice per group for the MERS-CoV therapeutic studies were as follows:  
525 Vehicle (n = 9), -2hr (n = 9), +12hr (n = 9), +24hr (n = 7), +48hr (n = 10). As described

526 above, each day mouse body weight and pulmonary function was quantitated. On 5dpi  
527 for SARS-CoV and 6dpi for MERS-CoV, animals were humanely sacrificed and tissues  
528 were harvested and analyzed as described above. In addition, for the MERS-CoV study,  
529 lung tissue was harvested and stored in RNAlater (Thermo Fisher) at -80°C and then  
530 thawed, homogenized in Trizol reagent (Invitrogen) and total RNA was isolated using a  
531 Direct-zol RNA MiniPrep kit (Zymo Research). This total RNA was then used for Primer  
532 ID and qRT-PCR.

533 **Whole body plethysmography.** Pulmonary function was monitored once daily via  
534 whole-body plethysmography (Buxco Respiratory Solutions, DSI Inc.). Mice destined for  
535 this analysis were chosen prior to infection. Briefly, after a 30-minute acclimation time in  
536 the plethysmograph, data for 11 parameters was recorded every 2 seconds for 5  
537 minutes.

538 **Acute lung injury histological assessment tools.** Two different and complementary  
539 quantitative histologic tools were used to determine if antiviral treatments diminished the  
540 histopathologic features associated with lung injury. Both analyses and scoring were  
541 performed by a Board Certified Veterinary Pathologist who was blinded to the treatment  
542 groups.

543 **American Thoracic Society Lung Injury Scoring Tool.** In order to help quantitate  
544 histological features of ALI observed in mouse models and increase their translation to  
545 the human condition, we used the ATS scoring tool<sup>49</sup>. In a blinded manner, we chose  
546 three random diseased fields of lung tissue at high power (60 ×), which were scored for  
547 the following: (A) neutrophils in the alveolar space (none = 0, 1–5 cells = 1, > 5 cells =  
548 2), (B) neutrophils in the interstitial space/ septae (none = 0, 1–5 cells = 1, > 5 cells = 2),  
549 (C) hyaline membranes (none = 0, one membrane = 1, > 1 membrane = 2), (D)  
550 Proteinaceous debris in air spaces (none = 0, one instance = 1, > 1 instance = 2), (E)  
551 alveolar septal thickening (< 2× mock thickness = 0, 2–4× mock thickness = 1, > 4×  
552 mock thickness = 2). To obtain a lung injury score per field, the scores for A–E were  
553 then put into the following formula, which contains multipliers that assign varying levels  
554 of importance for each phenotype of the disease state.: score = [(20x A) + (14 x B) + (7

555 x C) + (7 x D) + (2 x E)]/100. The scores for the three fields per mouse were averaged  
556 to obtain a final score ranging from 0 to and including 1.

557 **Diffuse Alveolar Damage (DAD) Tool.** The second histological tool to quantitate lung  
558 injury was reported by Schmidt et al.<sup>50</sup>. DAD is the pathological hallmark of ALI<sup>49,50</sup>.  
559 Three random diseased fields of lung tissue were score at high power (60 × ) for the  
560 following in a blinded manner: 1 = absence of cellular sloughing and necrosis, 2 =  
561 Uncommon solitary cell sloughing and necrosis (1–2 foci/field), 3 = multifocal (3 + foci)  
562 cellular sloughing and necrosis with uncommon septal wall hyalinization, or 4 =  
563 multifocal (>75% of field) cellular sloughing and necrosis with common and/or  
564 prominent hyaline membranes. The scores for the three fields per mouse were  
565 averaged to get a final DAD score per mouse.

566 **MERS-CoV genomic RNA qRT-PCR.** Mouse lungs were stored in RNAlater  
567 (ThermoFisher) at -80°C until processed via homogenization in TRIzol (Invitrogen).  
568 Total RNA was isolated using Direct-zol RNA MiniPrep kit (Zymo Research). Previously  
569 published TaqMan primers were synthesized by Integrated DNA Technologies (IDT) to  
570 quantify MERS genomic RNA (targeting orf1a. Forward: 5'-  
571 GCACATCTGTGGTTCTCCTCT-3', Probe (6-FAM/ZEN/IBFQ): 5'-  
572 TGCTCCAACAGTTACAC-3', Reverse: 5'-AAGCCCAGGCCCTACTATTAGC)<sup>51</sup>. qRT-  
573 PCR was performed using 100ng total RNA compared to an RNA standard curve using  
574 TaqMan Fast Virus 1-Step Master Mix (ThermoFisher) on a Quant Studio 3 (Applied  
575 Biosystems).

576 **nsp12 phylogenetic analysis and conservation modeling.** Coronavirus RdRp  
577 (nsp12) protein sequence alignments and phylogenetic trees were generated using  
578 Geneious Tree Builder in Geneious Prime (version 2020.0.5) and visualized using  
579 Evolview (<https://www.evolgenius.info/evolview/>). Protein similarity scores were  
580 calculated using Blosom62 matrix. The accession numbers used were : PDCoV  
581 (KR265858), AIBV (NC\_001451), HCoV-229E (JX503060), PEDV (NC\_003436), MHV  
582 (AY700211), HCoV-HKU1 (DQ415904), HCoV-NL63 (JX504050), HCOV-OC43  
583 (AY903460), HKU5-1 (NC\_009020), MERS-CoV (JX869059), HKU9-4 (EF065516),  
584 2019-nCoV (MN996528), HKU3-1 (DQ022305), SHC014 (KC881005), WIV1

585 (KF367457), SARS-CoV (AY278741). Amino acid conservation scores of coronavirus  
586 RdRp were generated using ConSurf Server (<https://consurf.tau.ac.il/>) using the protein  
587 alignment described above and visualized on the SARS-CoV RdRp structure (PDB:  
588 6NUR) in PyMol (version 1.8.6.0)<sup>20,52</sup>.

589 **Statistical analysis.** All statistical data analyses were performed in Graphpad Prism 8.  
590 Statistical significance for each endpoint was determined with specific statistical tests.  
591 For each test, a p-value <0.05 was considered significant. Specific tests are noted in  
592 each figure legend.

593 **Ethics regulation of laboratory animals.** Efficacy studies were performed in animal  
594 biosafety level 3 facilities at UNC Chapel Hill. All work was conducted under protocols  
595 approved by the Institutional Animal Care and Use Committee at UNC Chapel Hill  
596 (IACUC protocol #16-284) according to guidelines set by the Association for the  
597 Assessment and Accreditation of Laboratory Animal Care and the U.S. Department of  
598 Agriculture.

599

600 **Funding:** We would like to acknowledge the following funding sources, Antiviral Drug  
601 Discovery and Development Center (5U19AI109680), a partnership grant from the  
602 National Institutes of Health (5R01AI132178) and an NIAID R01 grant (AI108197). NIAID  
603 contract, HHSN272201500008C, was awarded to G.P. and The Emory institute for Drug  
604 Development and a subcontract from this was awarded to R.S.B. and M.R.D.

605

606 **Author contributions:** A.C.S., T.P.S, designed *in vitro* efficacy studies. A.C.S., A.J.B.,  
607 T.P.S. and R.L.G. executed and/or analyzed *in vitro* efficacy studies. J.H., A.T. and  
608 N.J.T. providing the clinical isolate of SARS-CoV-2. T.P.S., A.A.K., M.G.N., G.P. and  
609 R.S.B. designed *in vivo* efficacy studies. T.P.S., A.C.S., S.Z., C.S.H, and R.S. designed,  
610 executed and/or analyzed the Primer ID NGS data. K.H.D 3<sup>rd</sup> performed structural

611 modeling and phylogenetics and sequence alignments. M.L.A., A.J.P., J.D.C. and  
612 M.R.D. designed, performed and/or executed the construction of RDV resistant MHV  
613 and performed cross-resistance studies. T.P.S., A.S. and S.R.L. executed and analyzed  
614 *in vivo* efficacy studies. A.S. and S.R.L. performed whole body plethysmography for *in*  
615 *vivo* studies. S.A.M. assessed all lung pathology. G.R.B., and M.S., were responsible  
616 for synthesis, and scale-up of small molecules. T.P.S., A.C.S., S.Z., S.R.L, A.S., K.H.D.  
617 3<sup>rd</sup>, M.L.A., A.J.P., J.D.C, G.R.B., A.A.K., G.P., R.S. M.R.D., and R.S.B., wrote the  
618 manuscript.

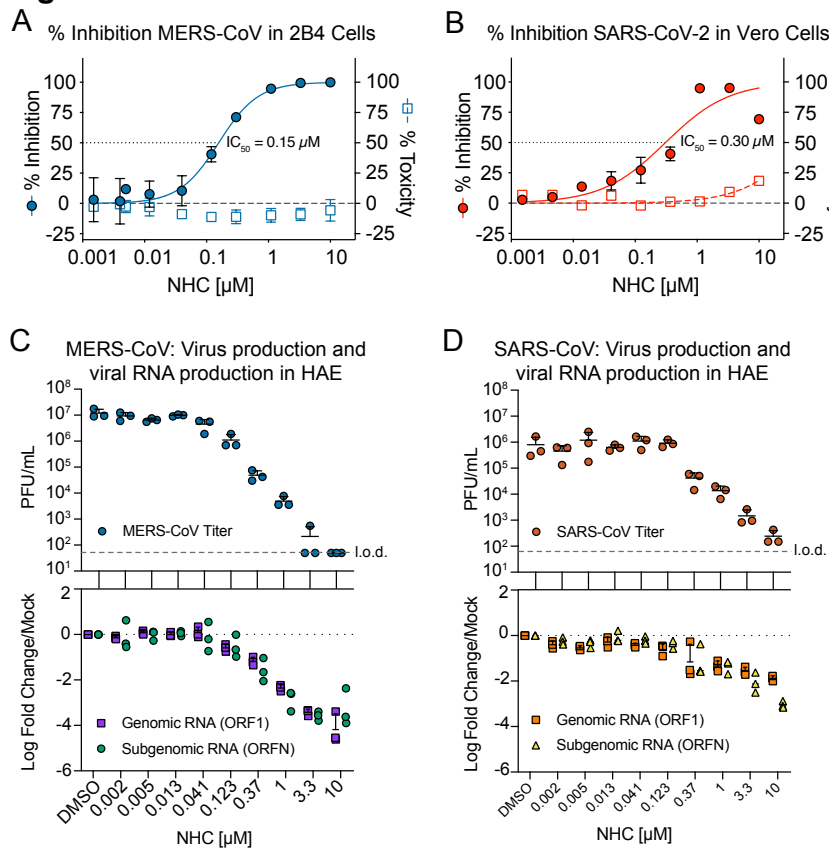
619 **Disclaimers**

620 The findings and conclusions in this report are those of the author(s) and do not  
621 necessarily represent the official position of the Centers for Disease Control and  
622 Prevention. Names of specific vendors, manufacturers, or products are included for  
623 public health and informational purposes; inclusion does not imply endorsement of the  
624 vendors, manufacturers, or products by the Centers for Disease Control and Prevention  
625 or the US Department of Health and Human Services.

626 **Competing financial interests:** A.C.S. received a contract from NIAID to support the *in*  
627 *vitro* and *in vivo* efficacy studies reported herein. UNC is pursuing IP protection for  
628 Primer ID and R.S. has received nominal royalties.

629

630 **Figures**



631

**Figure 1: NHC potently Inhibits MERS-CoV, SARS-CoV and newly emerging SARS-CoV-2**

**Replication.** **a**, NHC antiviral activity and cytotoxicity in Calu3 cells infected with MERS-CoV. Calu3 cells were infected in triplicate with MERS-CoV nanoluciferase (nLUC) at a multiplicity of infection (MOI) of 0.08 in the presence of a dose response of drug for 48 hours, after which replication was measured through quantitation of MERS-CoV-expressed nLUC. Cytotoxicity was measured in similarly treated but uninfected cultures via Cell-Titer-Glo assay. Data is combined from 3 independent experiments. **b**, NHC antiviral activity and cytotoxicity in Vero cells infected with SARS-CoV-2. Vero cells were infected in duplicate with SARS-CoV-2 clinical isolate virus at an MOI of 0.05 in the presence of a dose response of drug for 48 hours, after which replication was measured through quantitation of cell viability by Cell-Titer-Glo assay. Cytotoxicity was measured as in **a**. Data is combined from 2 independent experiments. **c**, NHC inhibits MERS-CoV virus production and RNA synthesis in primary human lung epithelial cell cultures (HAE). HAE cells were infected with MERS-CoV red fluorescent protein (RFP) at an MOI of 0.5 in duplicate in the presence of NHC for 48 hours, after which apical washes were collected for virus titration. qRT-PCR for MERS-CoV ORF1 and ORFN mRNA. Total RNA was isolated from cultures in **c** for qRT-PCR analysis. Representative data from three separate experiments with three different cell donors are displayed. PFU, plaque-forming units. **d**, NHC inhibits SARS-CoV virus production and RNA synthesis in primary human lung epithelial cell cultures (HAE). Studies performed as in **c** but with SARS-CoV green fluorescent protein (GFP). Representative data from two separate experiments with two different cell donors are displayed.

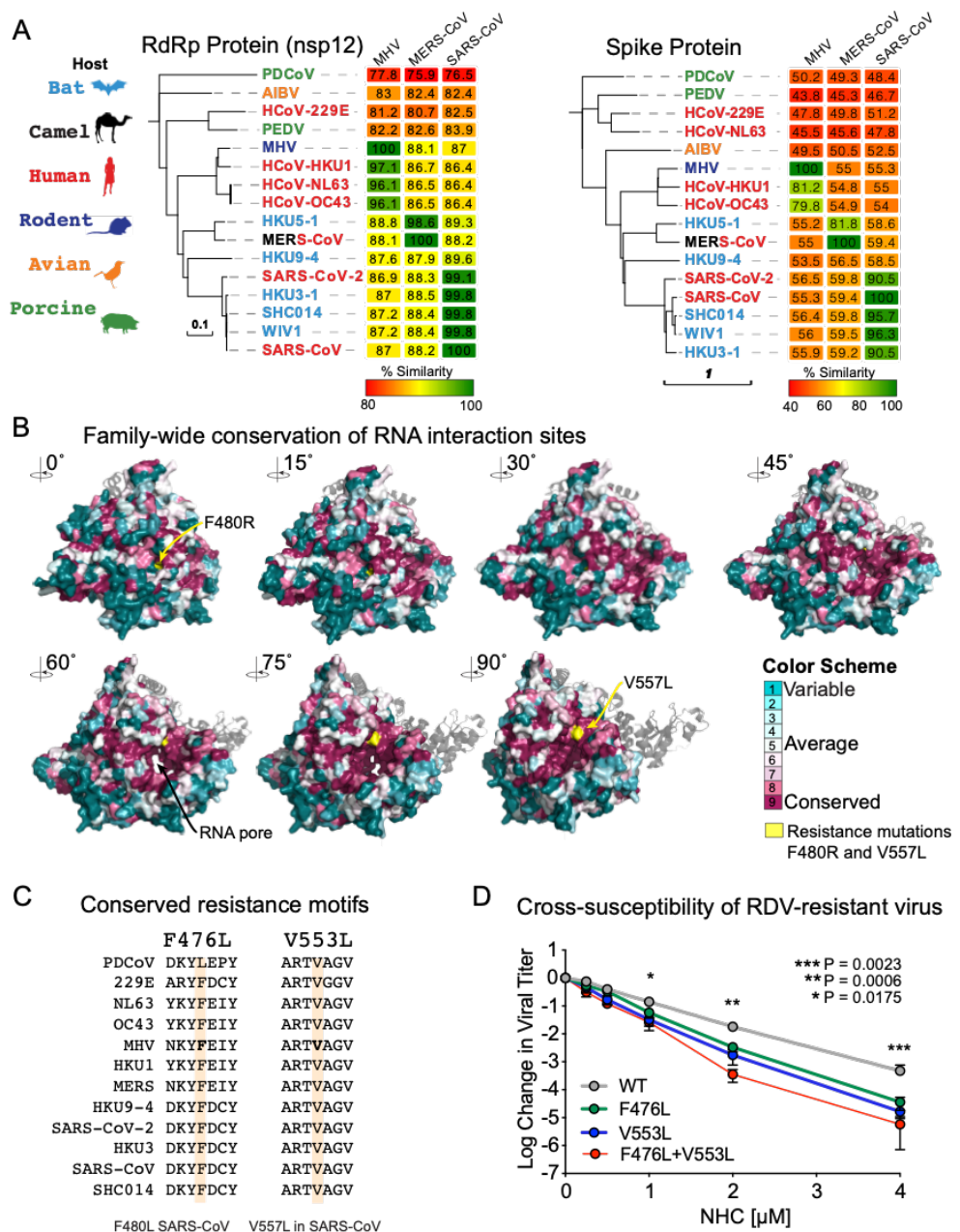
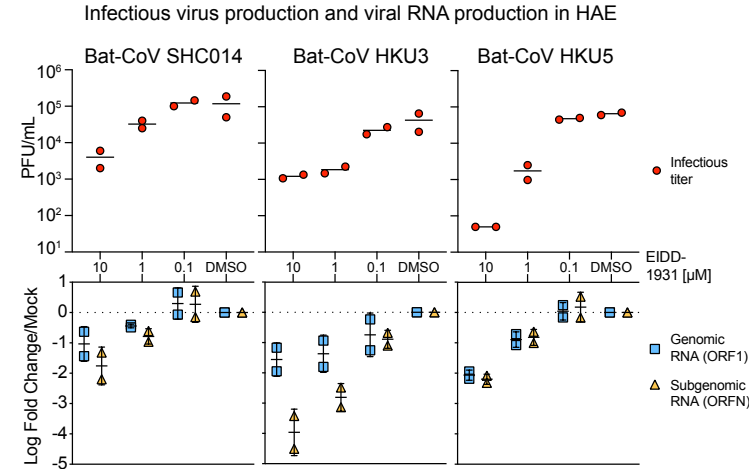


Figure 2

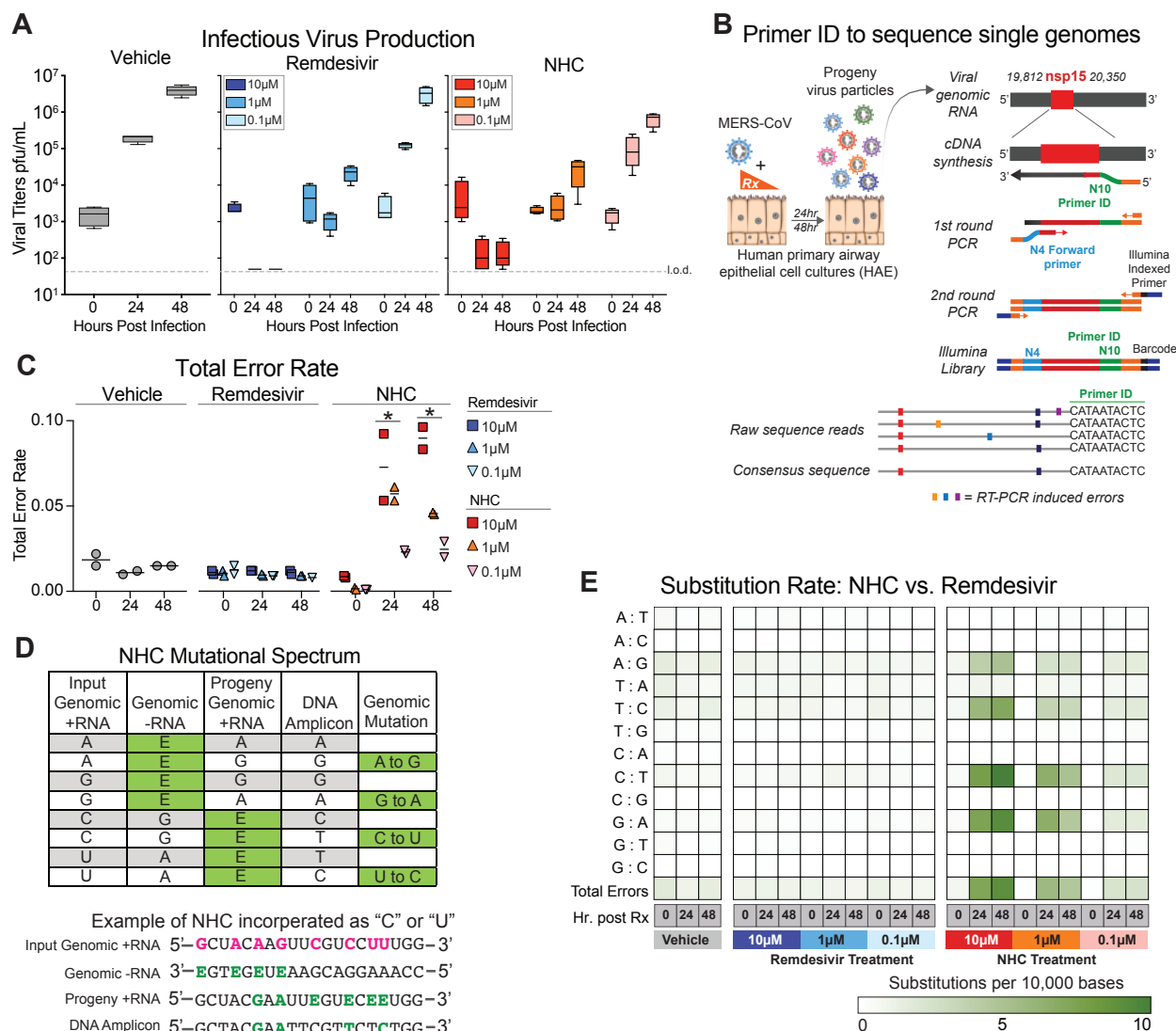
651  
652 **Figure 2. Remdesivir resistance mutations in the highly conserved RNA-dependent RNA**  
653 **polymerase increase susceptibility to NHC.** **a**, Neighbor-joining trees created with representatives from  
654 all four CoV genogroups showing the genetic similarity of CoV nsp12 (RdRp) and CoV spike glycoprotein,  
655 which mediates host tropism and entry into cells. Text color of the virus strain label corresponds to virus  
656 host species on the left. The heatmap adjacent to each neighbor-joining tree depicts percent amino acid  
657 identity (% A.A. similarity) against mouse hepatitis virus (MHV), SARS-CoV or MERS-CoV. **b**, Core  
658 residues of the CoV RdRp are highly conserved among CoV. The variation encompassed in panel **a** was  
659 modeled onto the RdRp structure of the SARS-CoV RdRp. **c**, Amino acid sequence of CoV in panel **a** at  
660 known resistance alleles to antiviral drug remdesivir (RDV). **d**, RDV resistant viruses are more susceptible  
661 to NHC antiviral activity. Virus titer reduction assay across a dose response of NHC with recombinant  
662 MHV bearing resistance mutations to RDV. Asterisks indicate statistically significant differences by Mann-  
663 Whitney test.

664

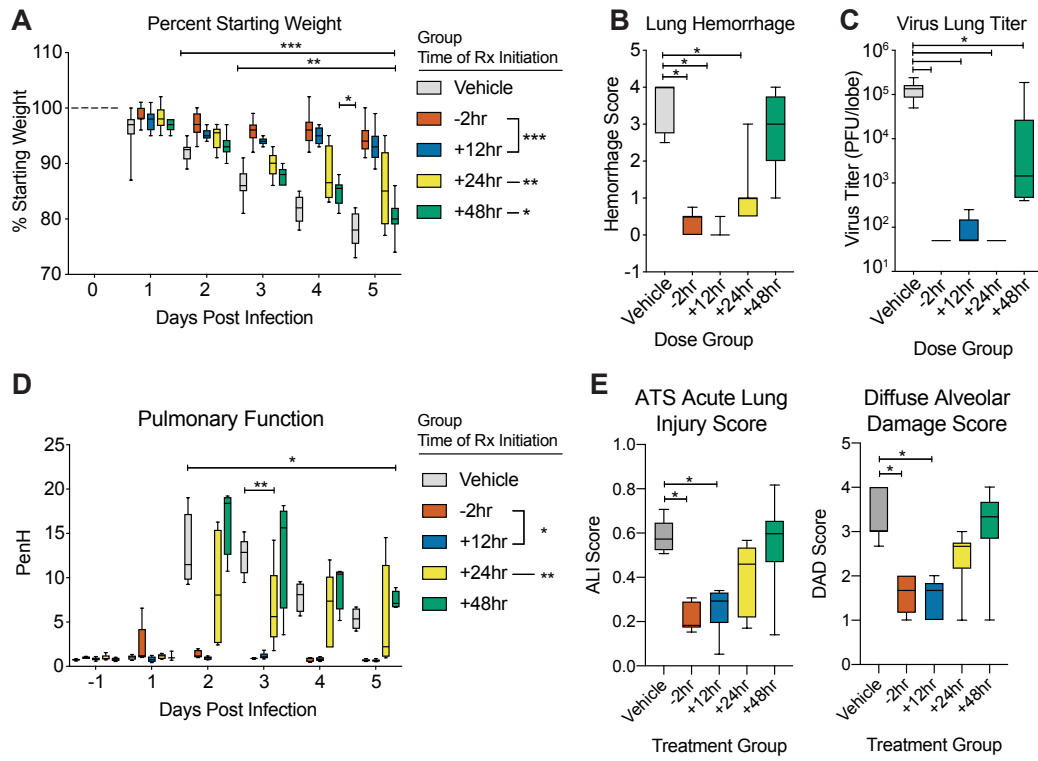


665  
666  
667  
668  
669  
670  
671

**Figure 3: NHC is effective against multiple genetically distinct Bat-CoV.** Top: Antiviral efficacy of NHC in HAE cells against SARS-like (HKU3, SHC014, group 2b) and MERS-like (HKU5, group 2c) bat-CoV. HAE cells were infected at an MOI of 0.5 in the presence of NHC in duplicate. After 48 hours, virus produced was titrated via plaque assay. Each data point represents the titer per culture. Bottom: qRT-PCR for CoV ORF1 and ORFN mRNA in total RNA from cultures in the top panel. Representative data from two separate experiments with two different cell donors are displayed.



672  
673 **Figure 4: NHC antiviral activity is associated with increased viral mutation rates.** **a**, Both remdesivir  
674 (RDV) and NHC reduce MERS-CoV infectious virus production in primary human HAE. Cultures were  
675 infected with MERS-CoV red fluorescent protein (RFP) at an MOI of 0.5 in duplicate in the presence of  
676 vehicle, RDV or NHC for 48 hours, after which apical washes were collected for virus titration. Data is  
677 combined from two independent studies. **b**, A deep sequencing approach called Primer ID to gain  
678 accurate sequence data for single RNA genomes of MERS-CoV. **c**, The total error rate for MERS-CoV  
679 RNA isolated from cultures in panel **a** as determined by Primer ID. Error rate values are # mutations per  
680 10,000 bases. Asterisks indicate significant differences as compared to untreated by 2-way ANOVA with  
681 a Dunnett's multiple comparison test. **d**, description of potential NHC mutational spectra on both positive  
682 and negative sense viral RNA. **e**, Nucleotide transitions adenine (A) to guanine (G) and uridine (U) to  
683 cytosine (C) transitions are enriched in MERS-CoV genomic RNA in an NHC dose dependent manner.  
684



685  
686  
687  
688  
689  
690  
691  
692  
693  
694  
695  
696  
697  
698  
699  
700  
701  
702  
703  
704

**Figure 5: Prophylactic and Therapeutic EIDD-2801 reduces SARS-CoV replication and pathogenesis.** Equivalent numbers of 25-29 week old male and female C57BL/6 mice were administered vehicle (10% PEG, 2.5% Cremophor RH40 in water) or NHC prodrug EIDD-2801 beginning at -2hr, +12, +24 or +48hr post infection and every 12hr thereafter by oral gavage (n = 10/group). Mice were intranasally infected with 1E+04 PFU mouse-adapted SARS-CoV MA15 strain. **a**, Percent starting weight. Asterisks indicate differences by two-way ANOVA with Tukey's multiple comparison test. **b**, Lung hemorrhage in mice from panel **a** scored on a scale of 0-4 where 0 is a normal pink healthy lung and 4 is a diffusely discolored dark red lung. **c**, Virus lung titer in mice from panel **a** as determined by plaque assay. Asterisks in both panel **b** and **c** indicate differences by one-way ANOVA with a Dunnett's multiple comparison test. **d**, Pulmonary function by whole body plethysmography was performed daily on five animals per group. Asterisks indicate differences by two-way ANOVA with a Dunn's multiple comparison test. **e**, Therapeutic EIDD-2801 reduces acute lung injury (ALI). The histological features of ALI were blindly scored using the American Thoracic Society Lung Injury Scoring system and a Diffuse Alveolar Damage Scoring System. Three randomly chosen high power (60X) fields of diseased lung were assessed per mouse. The numbers of mice scored per group: Vehicle N = 7, -2hr N = 9, +12hr N = 9, +24hr N = 10, +48hr N = 9. Asterisks indicate statistical significance by Kruskal-Wallis with a Dunn's multiple comparison test. For all panels, the boxes encompass the 25th to 75th percentile, the line is at the median, while the whiskers represent the range.

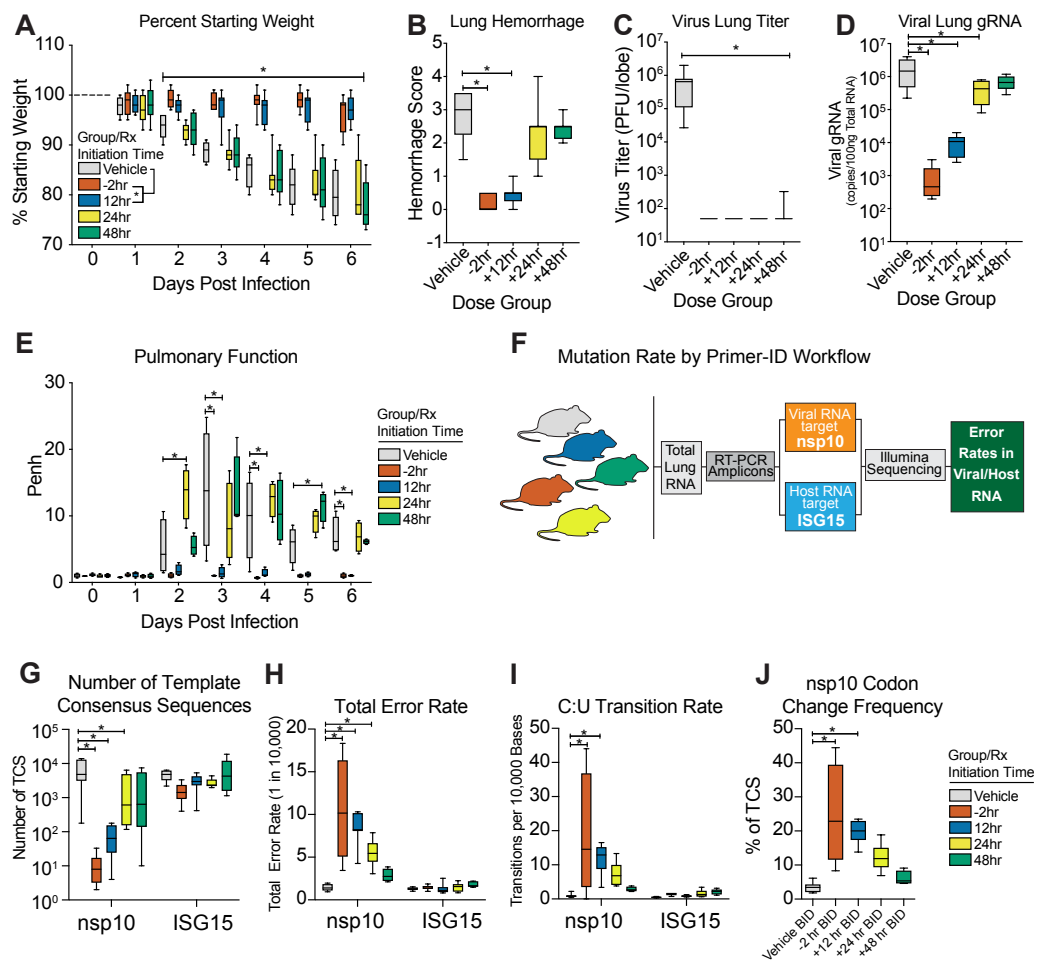
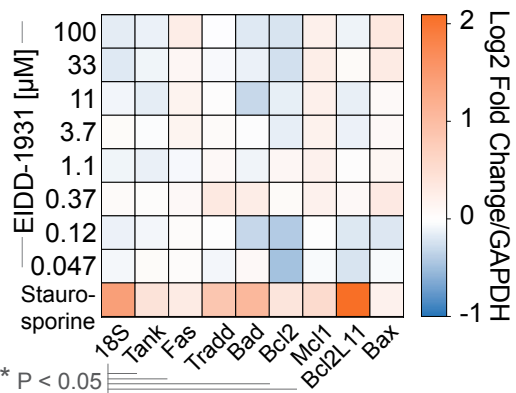


**Figure 6: Prophylactic and therapeutic EIDD-2801 reduces MERS-CoV replication and pathogenesis coincident with increased viral mutation rates.** Equivalent numbers of 10-14 week old male and female C57BL/6 hDPP4 mice were administered vehicle (10% PEG, 2.5% Cremophor RH40 in water) or NHC prodrug EIDD-2801 beginning at -2hr, +12, +24 or +48hr post infection and every 12hr thereafter by oral gavage (n = 10/group). Mice were intranasally infected with 5E+04 PFU mouse-adapted MERS-CoV M35C4 strain. **a**, Percent starting weight. Asterisks indicate differences by two-way ANOVA with Tukey's multiple comparison test. **b**, Lung hemorrhage in mice from panel **a** scored on a scale of 0-4 where 0 is a normal pink healthy lung and 4 is a diffusely discolored dark red lung. **c**, Virus lung titer in mice from panel **a** as determined by plaque assay. Asterisks in both panel **b** and **c** indicate differences by Kruskal-Wallis with Dunn's multiple comparison test. **d**, MERS-CoV genomic RNA in lung tissue by qRT-PCR. Asterisks indicate differences by one-way ANOVA with a Dunnett's multiple comparison test. **e**, Pulmonary function by whole body plethysmography was performed daily on four animals per group. Asterisks indicate differences by two-way ANOVA with Tukey's multiple comparison test. **f**, Workflow to measure mutation rate in MERS-CoV RNA and host transcript ISG15 by Primer ID in mouse lung tissue. **g**, Number of template consensus sequences for MERS-CoV nsp10 and ISG15. **h**, Total error rate in MERS-CoV nsp10 and ISG15. **i**, The cytosine to uridine transition rate in MERS-CoV nsp10 and ISG15. In panels **g-i**, asterisks indicate differences by two-way ANOVA with Tukey's multiple comparison test. **j**, Codon change frequency in MERS-CoV nsp10. Asterisks indicate differences on Kruskal-Wallis with Dunn's multiple comparison test.

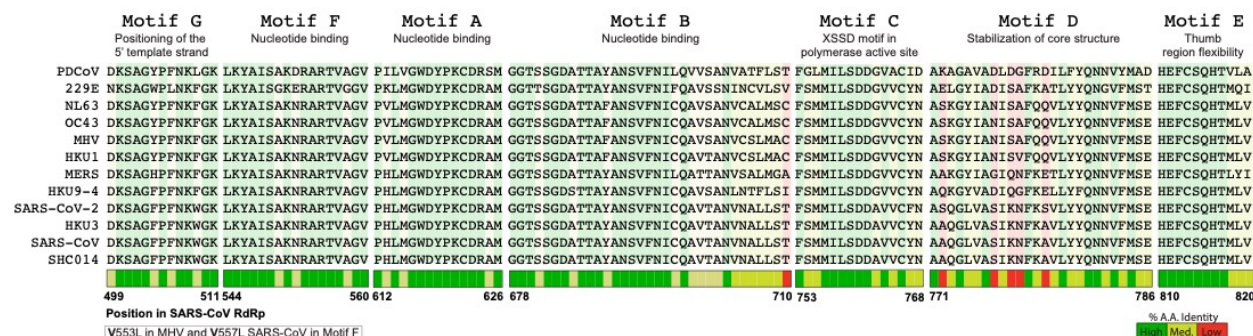
### Cell death factor expression in HAE



725  
726  
727  
728  
729  
730  
731  
732  
733

**Supplementary Figure 1: Assessment of cytotoxicity of NHC in primary human epithelial cell cultures by qRT-PCR.** Companion figure to **Figure 1c and d.** Primary human epithelial cell cultures were exposed to positive control 1 μM staurosporine or a dose response of NHC for 48hr. Cytotoxicity was assessed by qRT-PCR for cell death factor gene expression.

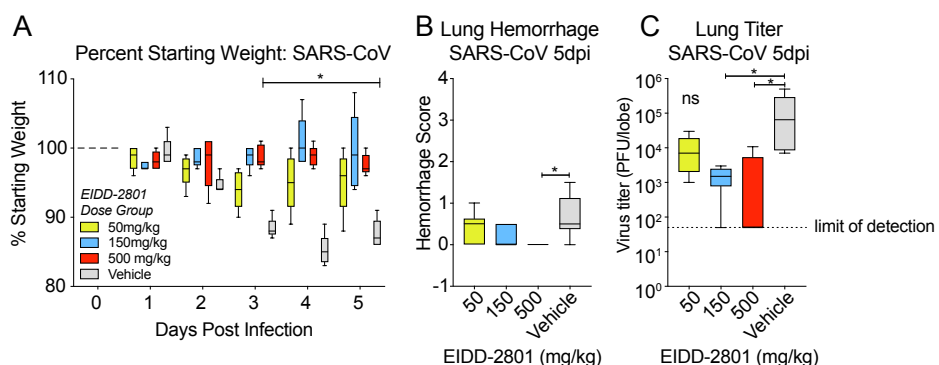
### Conservation of key RdRp motif residues



734  
735  
736  
737  
738  
739  
740

**Supplementary Figure 2: High conservation of RdRp functional domains for SARS-CoV-2.** Companion figure to **Figure 2a.** Multiple sequence alignment of the RNA dependent RNA polymerase (RdRp) from viruses in the dendrogram in Figure 2a showing high conservation in the RdRp structural motifs A-G.

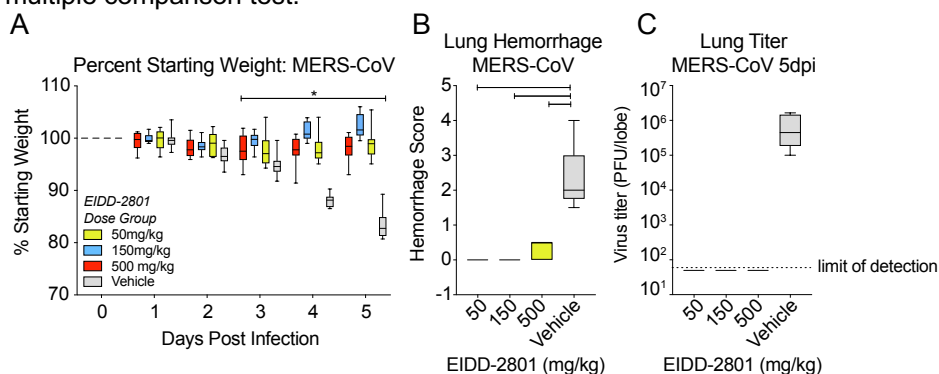
741



742

### Supplementary Figure 3: Prophylactic EIDD-2801 reduces SARS-CoV replication and

pathogenesis. Companion figure to **Figure 5**. Equivalent numbers of 20 week old male and female C57BL/6 mice were administered vehicle (10% PEG, 2.5% Cremophor RH40 in water) or NHC prodrug EIDD-2801 beginning at 2hr prior to infection and every 12hr thereafter by oral gavage (n = 10/group). Mice were intranasally infected with 1E+04 PFU mouse-adapted SARS-CoV MA15 strain. **a**, Percent starting weight. Asterisks indicate differences by two-way ANOVA with Dunnett's multiple comparison test. **b**, Lung hemorrhage in mice from panel **a** scored on a scale of 0-4 where 0 is a normal pink healthy lung and 4 is a diffusely discolored dark red lung. **c**, Virus lung titer in mice from panel **a** as determined by plaque assay. Asterisks in both panel **b** and **c** indicate differences by Kruskal-Wallis with a Dunn's multiple comparison test.



753

### Supplementary Figure 4: Prophylactic EIDD-2801 reduces MERS-CoV replication and

pathogenesis. Companion figure to **Figure 6**. Equivalent numbers of 10-14 week old male and female C57BL/6 hDPP4 mice were administered vehicle (10% PEG, 2.5% Cremophor RH40 in water) or NHC prodrug EIDD-2801 beginning 2hr prior to infection every 12hr thereafter by oral gavage (n = 10/group). Mice were intranasally infected with 5E+04 PFU mouse-adapted MERS-CoV M35C4 strain. **a**, Percent starting weight. Asterisks indicate differences by two-way ANOVA with Dunnett's multiple comparison test. **b**, Lung hemorrhage in mice from panel **a** scored on a scale of 0-4 where 0 is a normal pink healthy lung and 4 is a diffusely discolored dark red lung. **c**, Virus lung titer in mice from panel **a** as determined by plaque assay. Asterisks in both panel **b** and **c** indicate differences by Kruskal-Wallis with Dunn's multiple comparison test.

**Supplementary Table 1. Real-time PCR primer/probe sets for indicators of cellular apoptosis/toxicity**

Primer/Probe Target	Assay Reference Number*
Bax	Hs00180269_m1
Bad	Hs00188930_m1
Bcl2L11	Hs00708019_s1
Bcl2	Hs00608023_m1
Mcl1	Hs01050896_m1
Tradd	Hs00601065_g1
Fas	Hs00236330_m1
Tank	Hs00370305_m1
18S	4352930E
GAPD**	4352934E

\* Validated assays available from Life Technologies

\*\* The housekeeping gene hGAPDH was used for normalization of real-time results.

**Supplementary Table 2. Primer used for MiSeq library prep and sequencing.**

Primer	5'-3'	Comment
41R_PID11	GTGACTGGAGTTCAGACGTGTGCTTCCGATCTNNNNNNNNNNNC AGTATGACCTTCCTGTTGCTTCT	cDNA primer. Targeting 20331-20350 on the reference genome.
nsp10_PID11	GTGACTGGAGTTCAGACGTGTGCTTCCGATCTNNNNNNNNNNNC AGTCCTAACAGACGACATCAGTGG	cDNA primer. Targeting 13488-13507 on the reference genome.
nsp12_PID11	GTGACTGGAGTTCAGACGTGTGCTTCCGATCTNNNNNNNNNNNC AGTATAGCCAAAGACACAAACCG	cDNA primer. Targeting 15983-16002 on the reference genome.
nsp14_PID11	GTGACTGGAGTTCAGACGTGTGCTTCCGATCTNNNNNNNNNNNC AGTGAACATCGACAAAGAAAGGG	cDNA primer. Targeting 18715-18734 on the reference genome.
ifit3_PID11	GTGACTGGAGTTCAGACGTGTGCTTCCGATCTNNNNNNNNNNNC AGTTCAAGCCACTCCTTATCC	cDNA primer. Targeting mice IFIT3 mRNA.
isg15_PID11	GTGACTGGAGTTCAGACGTGTGCTTCCGATCTNNNNNNNNNNNC AGTGGGGCTTCTAGGCCATACTC	cDNA primer. Targeting mice ISG15 mRNA.
41F_AD	GCCTCCCTCGCGCCATCAGAGATGTGTATAAGAGACAGNNNNCTA CAAGTCGTCCTTGG	1 <sup>st</sup> round PCR forward primer. Targeting 19812-19831 on the reference genome
nsp10_AD	GCCTCCCTCGCGCCATCAGAGATGTGTATAAGAGACAGNNNTGCT CAGGTGCTAACGGAAT	1 <sup>st</sup> round PCR forward primer. Targeting 12983-13002 on the reference genome
nsp12_AD	GCCTCCCTCGCGCCATCAGAGATGTGTATAAGAGACAGNNNATAG GCTTCGATGTTGAGGG	1 <sup>st</sup> round PCR forward primer. Targeting 15388-15407 on the reference genome
nsp14_AD	GCCTCCCTCGCGCCATCAGAGATGTGTATAAGAGACAGNNNNATTG CAAGCTGGTTCAACA	1 <sup>st</sup> round PCR forward primer. Targeting 18260-18279 on the reference genome
ifit3_AD	GCCTCCCTCGCGCCATCAGAGATGTGTATAAGAGACAGNNNCGAT CCACAGTAAACAAACAG	1 <sup>st</sup> round PCR forward primer. Targeting mice IFIT3 mRNA.
isg15_AD	GCCTCCCTCGCGCCATCAGAGATGTGTATAAGAGACAGNNNTGG GACCTAAAGGTGAAGATG	1 <sup>st</sup> round PCR forward primer. Targeting mice ISG15 mRNA.
Adapter R	GTGACTGGAGTTCAGACGTGTGCTC	1 <sup>st</sup> round PCR reverse primer
Universal Adapter	AATGATACGGCGACCACCGAGATCTACACGCCCTCGCGCCATC AGAGATGTG	2 <sup>nd</sup> round PCR forward primer with Illumina adapter sequence
Indexed Adapter	CAAGCAGAACGGCATACGAGATNNNNNNGTACTGGAGTTCA ACGTGTGCTC	2 <sup>nd</sup> round PCR reverse primer with Illumina adapter sequence and indices (NNNNNNNN)
Old Nextera	GCCTCCCTCGCGCCATCAGAGATGTGTATAAGAGACAG	Customized sequencing primer

768 1. WHO. Middle East respiratory syndrome coronavirus (MERS-CoV). (2018).  
769 2. de Wit, E., van Doremalen, N., Falzarano, D. & Munster, V.J. SARS and MERS:  
770 recent insights into emerging coronaviruses. *Nat Rev Microbiol* **14**, 523-534  
771 (2016).  
772 3. Wang, D., et al. Clinical Characteristics of 138 Hospitalized Patients With 2019  
773 Novel Coronavirus-Infected Pneumonia in Wuhan, China. *JAMA* (2020).  
774 4. Zaki, A.M., van Boheemen, S., Bestebroer, T.M., Osterhaus, A.D. & Fouchier,  
775 R.A. Isolation of a novel coronavirus from a man with pneumonia in Saudi Arabia.  
776 *N Engl J Med* **367**, 1814-1820 (2012).  
777 5. Hsu, L.Y., et al. Severe acute respiratory syndrome (SARS) in Singapore: clinical  
778 features of index patient and initial contacts. *Emerg Infect Dis* **9**, 713-717 (2003).  
779 6. Zhou, P., et al. Fatal swine acute diarrhoea syndrome caused by an HKU2-  
780 related coronavirus of bat origin. *Nature* **556**, 255-258 (2018).  
781 7. Woo, P.C., et al. Molecular diversity of coronaviruses in bats. *Virology* **351**, 180-  
782 187 (2006).  
783 8. Menachery, V.D., et al. A SARS-like cluster of circulating bat coronaviruses  
784 shows potential for human emergence. *Nat Med* **21**, 1508-1513 (2015).  
785 9. Menachery, V.D., et al. SARS-like WIV1-CoV poised for human emergence. *Proc  
786 Natl Acad Sci U S A* **113**, 3048-3053 (2016).  
787 10. Reynard, O., et al. Identification of a New Ribonucleoside Inhibitor of Ebola Virus  
788 Replication. *Viruses* **7**, 6233-6240 (2015).  
789 11. Urakova, N., et al. beta-d-N (4)-Hydroxycytidine Is a Potent Anti-alphavirus  
790 Compound That Induces a High Level of Mutations in the Viral Genome. *J Virol*  
791 **92**(2018).  
792 12. Toots, M., et al. Characterization of orally efficacious influenza drug with high  
793 resistance barrier in ferrets and human airway epithelia. *Sci Transl Med*  
794 **11**(2019).  
795 13. Agostini, M.L., et al. Small-Molecule Antiviral beta-d-N (4)-Hydroxycytidine  
796 Inhibits a Proofreading-Intact Coronavirus with a High Genetic Barrier to  
797 Resistance. *J Virol* **93**(2019).  
798 14. Jordan, P.C., et al. Initiation, extension, and termination of RNA synthesis by a  
799 paramyxovirus polymerase. *PLoS Pathog* **14**, e1006889 (2018).  
800 15. Sheahan, T.P., et al. Comparative therapeutic efficacy of remdesivir and  
801 combination lopinavir, ritonavir, and interferon beta against MERS-CoV. *Nat  
802 Commun* **11**, 222 (2020).  
803 16. Sheahan, T.P., et al. Broad-spectrum antiviral GS-5734 inhibits both epidemic  
804 and zoonotic coronaviruses. *Sci Transl Med* **9**(2017).  
805 17. Anthony, S.J., et al. Further Evidence for Bats as the Evolutionary Source of  
806 Middle East Respiratory Syndrome Coronavirus. *mBio* **8**(2017).  
807 18. Hu, B., Ge, X., Wang, L.F. & Shi, Z. Bat origin of human coronaviruses. *Virol J*  
808 **12**, 221 (2015).  
809 19. Huynh, J., et al. Evidence supporting a zoonotic origin of human coronavirus  
810 strain NL63. *J Virol* **86**, 12816-12825 (2012).  
811 20. Kirchdoerfer, R.N. & Ward, A.B. Structure of the SARS-CoV nsp12 polymerase  
812 bound to nsp7 and nsp8 co-factors. *Nat Commun* **10**, 2342 (2019).

813 21. Agostini, M.L., *et al.* Coronavirus Susceptibility to the Antiviral Remdesivir (GS-  
814 5734) Is Mediated by the Viral Polymerase and the Proofreading  
815 Exoribonuclease. *MBio* **9**(2018).

816 22. Becker, M.M., *et al.* Synthetic recombinant bat SARS-like coronavirus is  
817 infectious in cultured cells and in mice. *Proc Natl Acad Sci U S A* **105**, 19944-  
818 19949 (2008).

819 23. Agnihothram, S., *et al.* A mouse model for Betacoronavirus subgroup 2c using a  
820 bat coronavirus strain HKU5 variant. *MBio* **5**, e00047-00014 (2014).

821 24. Yoon, J.J., *et al.* Orally Efficacious Broad-Spectrum Ribonucleoside Analog  
822 Inhibitor of Influenza and Respiratory Syncytial Viruses. *Antimicrob Agents  
823 Chemother* **62**(2018).

824 25. Zhou, S., Jones, C., Mieczkowski, P. & Swanstrom, R. Primer ID Validates  
825 Template Sampling Depth and Greatly Reduces the Error Rate of Next-  
826 Generation Sequencing of HIV-1 Genomic RNA Populations. *J Virol* **89**, 8540-  
827 8555 (2015).

828 26. Tchesnokov, E.P., Feng, J.Y., Porter, D.P. & Gotte, M. Mechanism of Inhibition of  
829 Ebola Virus RNA-Dependent RNA Polymerase by Remdesivir. *Viruses* **11**(2019).

830 27. Menachery, V.D., Gralinski, L.E., Baric, R.S. & Ferris, M.T. New Metrics for  
831 Evaluating Viral Respiratory Pathogenesis. *PLoS One* **10**, e0131451 (2015).

832 28. Cockrell, A.S., *et al.* A mouse model for MERS coronavirus-induced acute  
833 respiratory distress syndrome. *Nat Microbiol* **2**, 16226 (2016).

834 29. Marston, H.D., Folkers, G.K., Morens, D.M. & Fauci, A.S. Emerging viral  
835 diseases: confronting threats with new technologies. *Sci Transl Med* **6**, 253ps210  
836 (2014).

837 30. Paules, C.I., Marston, H.D. & Fauci, A.S. Coronavirus Infections-More Than Just  
838 the Common Cold. *JAMA* (2020).

839 31. Brown, A.J., *et al.* Broad spectrum antiviral remdesivir inhibits human endemic  
840 and zoonotic deltacoronaviruses with a highly divergent RNA dependent RNA  
841 polymerase. *Antiviral Res* **169**, 104541 (2019).

842 32. Cai, B. Severe 2019-nCoV Remdesivir RCT (NCT04257656). (2020).

843 33. Ehteshami, M., *et al.* Characterization of beta-d-N(4)-Hydroxycytidine as a Novel  
844 Inhibitor of Chikungunya Virus. *Antimicrob Agents Chemother* **61**(2017).

845 34. Warren, T.K., *et al.* Therapeutic efficacy of the small molecule GS-5734 against  
846 Ebola virus in rhesus monkeys. *Nature* **531**, 381-385 (2016).

847 35. Lo, M.K., *et al.* GS-5734 and its parent nucleoside analog inhibit Filo-, Pneumo-,  
848 and Paramyxoviruses. *Sci Rep* **7**, 43395 (2017).

849 36. Oh, M.D., *et al.* Viral Load Kinetics of MERS Coronavirus Infection. *N Engl J Med*  
850 **375**, 1303-1305 (2016).

851 37. Peiris, J.S., *et al.* Clinical progression and viral load in a community outbreak of  
852 coronavirus-associated SARS pneumonia: a prospective study. *Lancet* **361**,  
853 1767-1772 (2003).

854 38. de Wit, E., *et al.* Middle East respiratory syndrome coronavirus (MERS-CoV)  
855 causes transient lower respiratory tract infection in rhesus macaques. *Proc Natl  
856 Acad Sci U S A* **110**, 16598-16603 (2013).

857 39. McAuliffe, J., *et al.* Replication of SARS coronavirus administered into the  
858 respiratory tract of African Green, rhesus and cynomolgus monkeys. *Virology*  
859 **330**, 8-15 (2004).

860 40. Zumla, A., Chan, J.F., Azhar, E.I., Hui, D.S. & Yuen, K.Y. Coronaviruses - drug  
861 discovery and therapeutic options. *Nat Rev Drug Discov* **15**, 327-347 (2016).

862 41. Smith, E.C., Blanc, H., Surdel, M.C., Vignuzzi, M. & Denison, M.R.  
863 Coronaviruses lacking exoribonuclease activity are susceptible to lethal  
864 mutagenesis: evidence for proofreading and potential therapeutics. *PLoS Pathog*  
865 **9**, e1003565 (2013).

866 42. Sims, A.C., *et al.* Severe acute respiratory syndrome coronavirus infection of  
867 human ciliated airway epithelia: role of ciliated cells in viral spread in the  
868 conducting airways of the lungs. *J Virol* **79**, 15511-15524 (2005).

869 43. Scobey, T., *et al.* Reverse genetics with a full-length infectious cDNA of the  
870 Middle East respiratory syndrome coronavirus. *Proc Natl Acad Sci U S A* **110**,  
871 16157-16162 (2013).

872 44. Douglas, M.G., Kocher, J.F., Scobey, T., Baric, R.S. & Cockrell, A.S. Adaptive  
873 evolution influences the infectious dose of MERS-CoV necessary to achieve  
874 severe respiratory disease. *Virology* **517**, 98-107 (2018).

875 45. Roberts, A., *et al.* A mouse-adapted SARS-coronavirus causes disease and  
876 mortality in BALB/c mice. *PLoS Pathog* **3**, e5 (2007).

877 46. Fulcher, M.L., Gabriel, S., Burns, K.A., Yankaskas, J.R. & Randell, S.H. Well-  
878 differentiated human airway epithelial cell cultures. *Methods Mol Med* **107**, 183-  
879 206 (2005).

880 47. Jabara, C.B., Jones, C.D., Roach, J., Anderson, J.A. & Swanstrom, R. Accurate  
881 sampling and deep sequencing of the HIV-1 protease gene using a Primer ID.  
882 *Proc Natl Acad Sci U S A* **108**, 20166-20171 (2011).

883 48. Fukushi, M., *et al.* Serial histopathological examination of the lungs of mice  
884 infected with influenza A virus PR8 strain. *PLoS One* **6**, e21207 (2011).

885 49. Matute-Bello, G., *et al.* An official American Thoracic Society workshop report:  
886 features and measurements of experimental acute lung injury in animals. *Am J  
887 Respir Cell Mol Biol* **44**, 725-738 (2011).

888 50. Schmidt, M.E., *et al.* Memory CD8 T cells mediate severe immunopathology  
889 following respiratory syncytial virus infection. *PLoS Pathog* **14**, e1006810 (2018).

890 51. Almazan, F., *et al.* Engineering a replication-competent, propagation-defective  
891 Middle East respiratory syndrome coronavirus as a vaccine candidate. *mBio* **4**,  
892 e00650-00613 (2013).

893 52. Ashkenazy, H., *et al.* ConSurf 2016: an improved methodology to estimate and  
894 visualize evolutionary conservation in macromolecules. *Nucleic Acids Res* **44**,  
895 W344-350 (2016).

896